

## Seasonal ice area and volume production of the Arctic Ocean: November 1996 through April 1997

R. Kwok and G. F. Cunningham

Jet Propulsion Laboratory, California Institute of Technology, Pasadena, California, USA

Received 31 May 2000; revised 20 December 2000; accepted 12 September 2001; published 14 September 2002.

[1] The RADARSAT Geophysical Processor System (RGPS) produces estimates of sea ice motion, deformation, and thickness of the Arctic Ocean sea ice cover from time-sequential synthetic aperture radar (SAR) imagery acquired by RADARSAT. Based on these products, we summarize the evolution of a region of the Arctic Ocean ice cover in terms of its area change, ice volume production, and multiyear ice coverage over a 6-month period between 7 November 1996 through 30 April 1997. This region encompasses a large part of the Western Arctic Ocean. The initial ice area covers  $\sim 2.52 \times 10^6$  km<sup>2</sup>. At the end of April, this region covers  $\sim 2.59 \times 10^6$  km<sup>2</sup>, a net divergence of  $\sim 3\%$ . Over the period, thin ice (0–20 cm) typically covers  $<2\%$  of this area. The RGPS estimates only the thickness distribution of sea ice volume produced by openings and closings of the ice cover since the initial observation. Thus, only the ice volume of the seasonal ice cover can be determined. Between November 1996 and April 1997,  $\sim 1000$  km<sup>3</sup> ( $\sim 0.4$  m) of sea ice is produced. The amount stored in undeformed ice and ridged ice is dependent on the character of the redistribution function. The RGPS products also provide estimates of multiyear ice coverage. From the time-series of multiyear ice coverage, we estimate that nearly 83% of the area is covered by multiyear ice. For more detailed examination of the regional dependence of ice-cover deformation, volume production, and MY ice coverage, the larger region is divided into five subregions. Where possible, we provide an analysis of the errors in the above estimates. In cases where quantification of the uncertainty is not feasible, we list the potential error sources. There are remaining sources of uncertainty in these calculations that remain unquantified, but at this time, there are no adequate in situ or remote-sensing data for comprehensive evaluation of the above estimates. *INDEX TERMS:* 4275 Oceanography: General: Remote sensing and electromagnetic processes (0689); 4207 Oceanography: General: Arctic and Antarctic oceanography; 4540 Oceanography: Physical: Ice mechanics and air/sea/ice exchange processes; 1640 Global Change: Remote sensing; 1620 Global Change: Climate dynamics (3309)

**Citation:** Kwok, R., and G. F. Cunningham, Seasonal ice area and volume production of the Arctic Ocean: November 1996 through April 1997, *J. Geophys. Res.*, 107(C10), 8038, doi:10.1029/2000JC000469, 2002.

### 1. Introduction

[2] At  $\sim 25$ – $100$  m resolution, synthetic aperture radar (SAR) imagery offers an amazingly detailed view of the sea ice cover. The observed radar backscatter is related to the physical properties that affect the scattering characteristics of the sea ice surface and volume. The magnitude of backscatter is a complex expression of the properties of the snow cover, the surface roughness of the snow-ice interface, the ice salinity, and the characteristics of the inhomogeneities (air bubbles, crystal size) in the ice volume. Earlier efforts at classification of radar data into age-related categories using simple backscatter-based algorithms [e.g., Kwok *et al.*, 1992] have limitations due to the overlapping signatures of ice types [Fetterer *et al.*, 1994; Steffen and Heirichs, 1994]. The most successful application of

SAR imagery for sea ice studies thus far, that takes advantage of its high spatial resolution, has been its use in the study of small-scale kinematics [Li *et al.*, 1995; Stern *et al.*, 1995; Overland *et al.*, 1998]. Ice motion is obtained by tracking common features in sequential radar imagery. However, the lack of large-scale spatially and temporally continuous SAR data confined these studies to small domains in time and space.

[3] The Canadian RADARSAT SAR was launched in November of 1995. The 24-day orbit cycle of the satellite and the wide-swath imaging mode of the C-band radar provide near repeat coverage of the entire Arctic Ocean every 3–6 days. In anticipation of these capabilities of RADARSAT, Kwok *et al.* [1995] suggested a scheme to use the available temporal and spatial coverage of the radar to obtain estimates of ice deformation and ice thickness from Lagrangian observations of ice motion. The motivation is to derive basin-scale estimates of geophysical fields that are suitable for process studies, model validation, and climato-

logical studies. The scheme follows Lagrangian elements of sea ice in time, thus allowing us to account for the history of area changes. Area changes are interpreted as openings and closings of the ice cover. In winter, openings are associated with the creation of open water areas which is then covered by young ice, while closings create rafted ice or pressure ridges. In conjunction with an ice growth model and a redistribution model, it is possible to estimate the seasonal ice thickness distribution within these elements. These two models represent the thermodynamic and dynamic processes involved in producing and maintaining ice of different thicknesses. From the observations of area and thickness estimates, we can compute the divergence of the ice cover and the volume stored in seasonal ice as a result of the formation of leads and ridges due to the nonuniform motion of sea ice. This scheme has been implemented in the RADARSAT Geophysical Processor System (RGPS), a data processing system designed to handle the large volumes of SAR imagery required to produce the basin-wide fields of ice motion and estimates of ice age and thickness from sequential maps of the Arctic Ocean. From the RGPS, we have for the first time routine estimates of one component of the thickness distribution - the seasonal ice produced by deformation of the ice cover.

[4] Beginning in November of 1996 and continuing today, we have been acquiring 3-day maps of the western Arctic Ocean within the Alaska SAR Facility (ASF) Reception mask in Fairbanks, Alaska. The repeat coverage of the Eurasian Basin is less frequent (6-days) due to the additional cost of RADARSAT data downlinked at the Tromsø Satellite Station in Norway. These data are used as inputs to the RGPS. At the time of this writing, the RGPS has completed the processing of one winter's worth of data.

[5] In this paper, we summarize the results from this winter - 7 November 1996 through 30 April 1997. These RGPS products are available on the Web (URL: <http://www-radar.jpl.nasa.gov/rgps/radarsat.html>). The discussions here focus on the area of the ice cover, volume production, and multiyear ice coverage. The uncertainty in each of these estimates is addressed to the extent possible with available observations from other studies and data sets. The paper is organized as follows. The next section provides a brief review of the algorithms used to estimate the seasonal ice thickness distribution based on the record of area change. We divide the ice cover into five subregions to examine the area changes, the volume production, and the MY-ice coverage in more detail. Section 3 discusses the area change and section 4 describes the volume production in the five subregions. The retrieval of MY ice coverage is discussed in section 5. The last section concludes the paper.

## 2. Data Description

### 2.1. Terminology/Algorithms

[6] The RGPS procedures estimate ice age and thickness from repeated observations of Lagrangian elements or cells of sea ice in sequential SAR imagery. We illustrate this process with an example. Figure 1 shows a sequence of observations of one cell within a matrix of such cells, the history of cell area, and the estimated seasonal ice thickness distribution at 12 selected time-steps over a period of 6 months. The nominal sampling period of the cell is  $\sim 3$

days, and is a limitation of the radar instrument and data acquisition scheme. The 12 time-steps are selected based on the activity (deformation) of that element. Line segments connecting the four vertices of a cell define its boundaries. The drift of a cell over time is obtained by tracking the displacement of its vertices in SAR imagery. The ice-tracking procedure is described by *Kwok et al.* [1995]. The decrease in cell area between Day 312 and 335 created ice ridges in the cell. Between Day 335 and 339, the opening of two new leads introduced a large area of open water and thus a category of thin ice between 0 and 4 days old. This is followed by more openings between Day 339 and 359. The cell is now covered with five different categories of sea ice in the 10–60 cm thick range. The series of closings after Day 359 ridged most of the thin ice in the cell. Only small changes in the cell area are evident after Day 30. At the end of the 171-day period, the largest category of undeformed ice is 1.5 m thick and occupies  $\sim 40\%$  of the initial area.

[7] An ice age histogram is constructed as an intermediate step in the estimation of ice thickness. The age histogram of the ice in a cell is computed from the temporal record of area changes. An age histogram of sea ice specifies the fractional area covered by ice of different chronological age. To construct this histogram from sequential observations, we follow the steps below. Each time a new cell observation becomes available, an increase in area is interpreted as the creation of an area of open water or young ice. If the air temperature is below freezing, new ice is assumed to grow over this area immediately after opening. The age uncertainty of the ice occupying this area is dependent on the length of the sampling interval. This uncertainty specifies an age range for this new ice area in the histogram. At the same time a new category is introduced, existing ice categories are “aged” chronologically by the same time interval. A decrease in area is assumed to have ridged the youngest ice in the cell, reducing its area. The procedure assumes that once ridging starts, the deformation tends to be localized in the recently formed younger and weaker ice in leads. This area of ridged ice is tracked as a separate category in the age histogram.

[8] Ice age is converted to ice thickness using an empirical ice growth formula. The growth rate is approximated as a function of the number of freezing-degree days associated with each age category using Lebedev's parameterization (discussed by *Maykut* [1986]) with  $h = 1.33 F^{0.58}$ , where  $h$  is thickness (cm) and  $F$  is the accumulated freezing-degree days ( $^{\circ}\text{K}$ ) derived from 2-m air temperature. This relationship is based on 24 station years of observations from various locations in the Soviet Arctic and describes ice growth under “average” snow conditions. Volume is conserved when ice is ridged. In pressure ridging, it is assumed that all ridged ice is five times its original thickness and occupies a quarter of its original area [*Parmerter and Coon*, 1972]. Pressure ridging and rafting are discussed in more detail in section 4.

[9] This scheme is initialized sometime after fall freeze-up by covering the entire Arctic Ocean with RGPS cells 10 km on a side. Coastal regions (within 100 km) are sampled by 25 km by 25 km elements as tracking ice features in these areas is more difficult. This selection is based solely on throughput considerations. Complete coverage of the

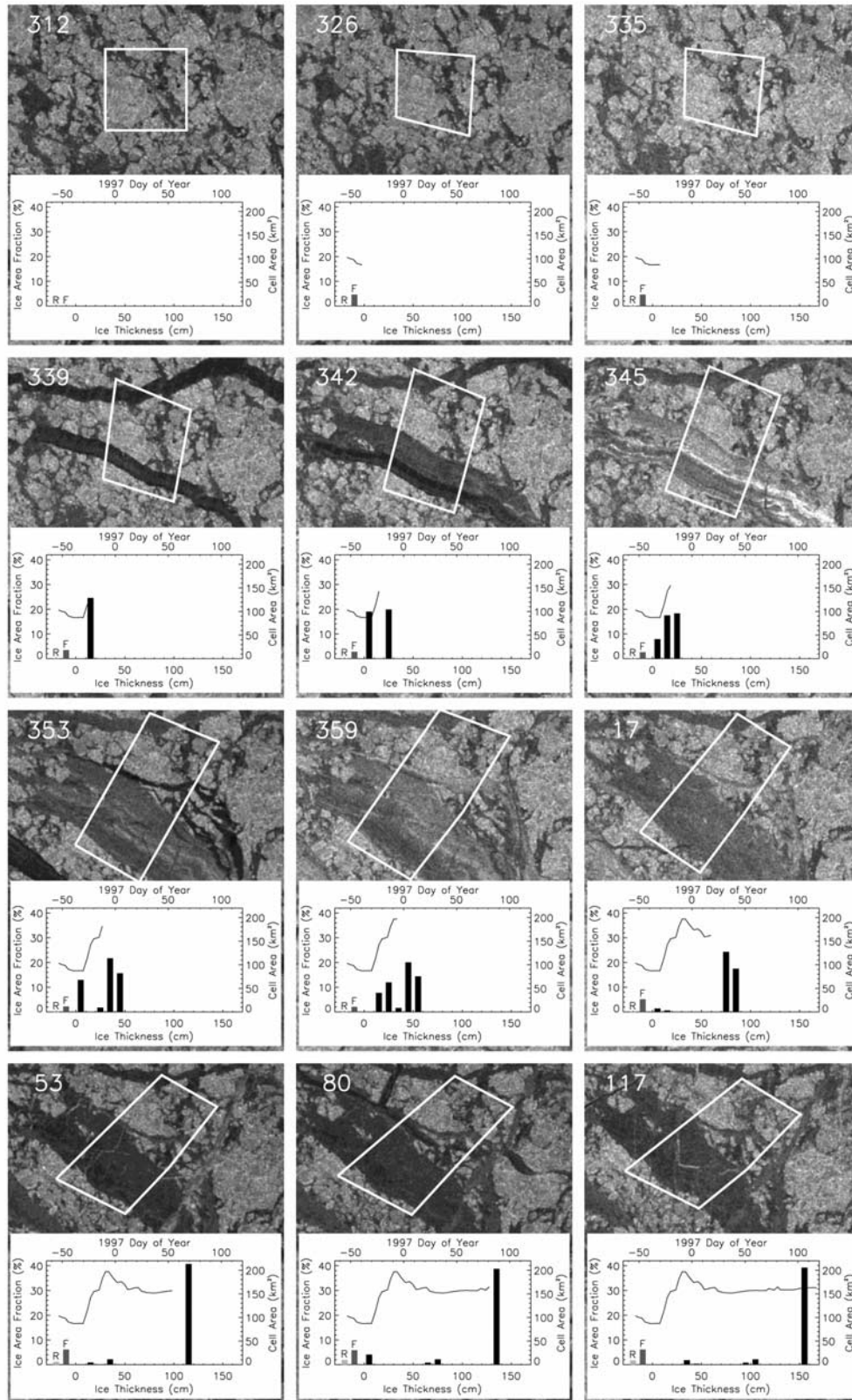


**Figure 1.** Sequence of observations of one RGPS cell (initially enclosed by a 10 km by 10 km square) in RADARSAT imagery. The plots show the area changes of a cell (solid line) and the seasonal ice thickness distribution (histogram) within the cell over a 171-day period. R and F represent the coverage of ridged ice and first-year ridges ( $F_Y$ ). The distinction between these two categories of deformed ice is discussed in section 4. The top/right axis-labels are associated with the area change curves; the bottom/left axis-labels are associated with the thickness histograms.

Arctic requires approximately 60,000 cells. At start up, the ice age/thickness distributions within the cells are unknown. In this process, the ice volume accumulated over the length of the RGPS record represents the seasonal ice volume produced by kinematics and thermodynamics since initialization. This ice thickness distribution,  $g_s(h)$ , includes only the seasonal undeformed ice and ridged ice. Since we do not melt ice in the scheme, the procedures above work only during the ice growth season. The results provide only one component of the entire age/thickness distribution, but this is the crucial thickness range that produces the most ice growth, the most turbulent heat flux to the atmosphere and the most salt flux to the ocean.

[10] The backscatter intensity of each SAR sample is used to provide an independent estimate of the multiyear (MY) fraction within each cell. The MY algorithm [Kwok *et al.*, 1995] uses a maximum likelihood classifier and a look-up table of expected MY-ice backscatter characteristics. An image pixel is assigned to one of two classes: multiyear ice and first-year ice. The assumption is that the area of MY ice over a region is near constant throughout the winter (by definition, no multiyear ice is created) with a small negative trend due to ridging. Any anomaly in the classification process due to the backscatter variability of other ice types would show up as transients or spikes in a time-series of retrieved MY-ice area. These anomalies can be filtered out in the time series of MY fraction estimates in each cell. The assumption of constant MY ice area is examined in section 5.

## 2.2. RGPS Observations (November 1996 through April 1997)

[11] We provide a brief summary of the RGPS products that span the 6 months between November 1996 and April 1997 here. Two sets of RGPS cell observations are used: deformation and ice thickness histogram. The ice deformation product contains the geographic location, the area, and the velocity gradients of each cell at every time step. A record of the derived thickness histograms and multiyear ice coverage estimates at these cells are stored in the ice thickness histogram product. The cells in this set of RGPS products sample only the ice-covered Arctic Ocean on November 1996 in the region east of  $135^\circ\text{E}$  and west of  $45^\circ\text{W}$ . Figure 2 shows the number of observations and average sampling period for cells within this region throughout the period, and the spatial coverage of the cells on 7 November 1996 and on 30 April 1997. There are no RGPS cells created over the sea ice formed after the initial date of 7 November 1996. Cells that are not observed throughout the entire period due to data acquisition gaps and ice-tracking difficulties appear as holes in the coverage map. Over the 6-month period, most of the cells have more than 60 observations or a sampling period of  $\sim 3$  days. As the ice drifts out of the ASF mask, the sampling frequency decreases. This is due to the different sampling strategy of the Arctic Ocean in the SAR data acquisition plan. Within the ASF reception mask the Arctic Ocean is covered every three days while outside the Alaska mask the sampling frequency degrades to once every 6 days.

[12] The cumulative deformation of the ice cover over the 6-month period as sampled by the RGPS cells is shown in Figure 3. The total deformation of each cell on 30 April 1997 is computed by first summing the velocity gradients

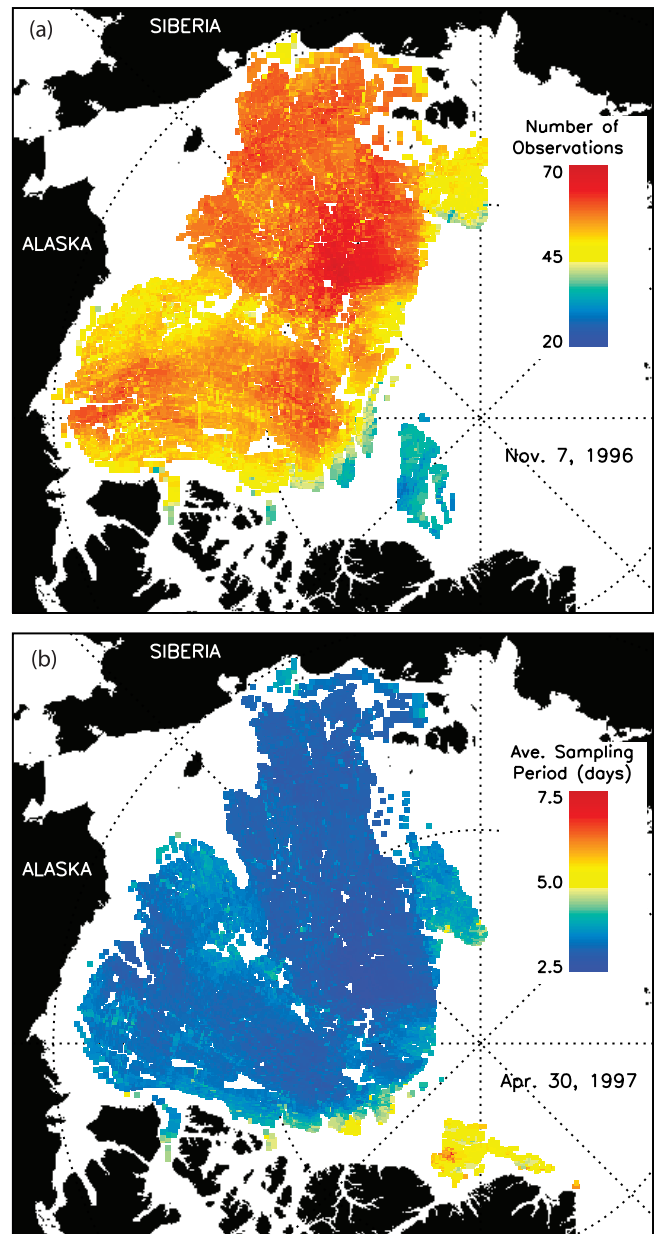
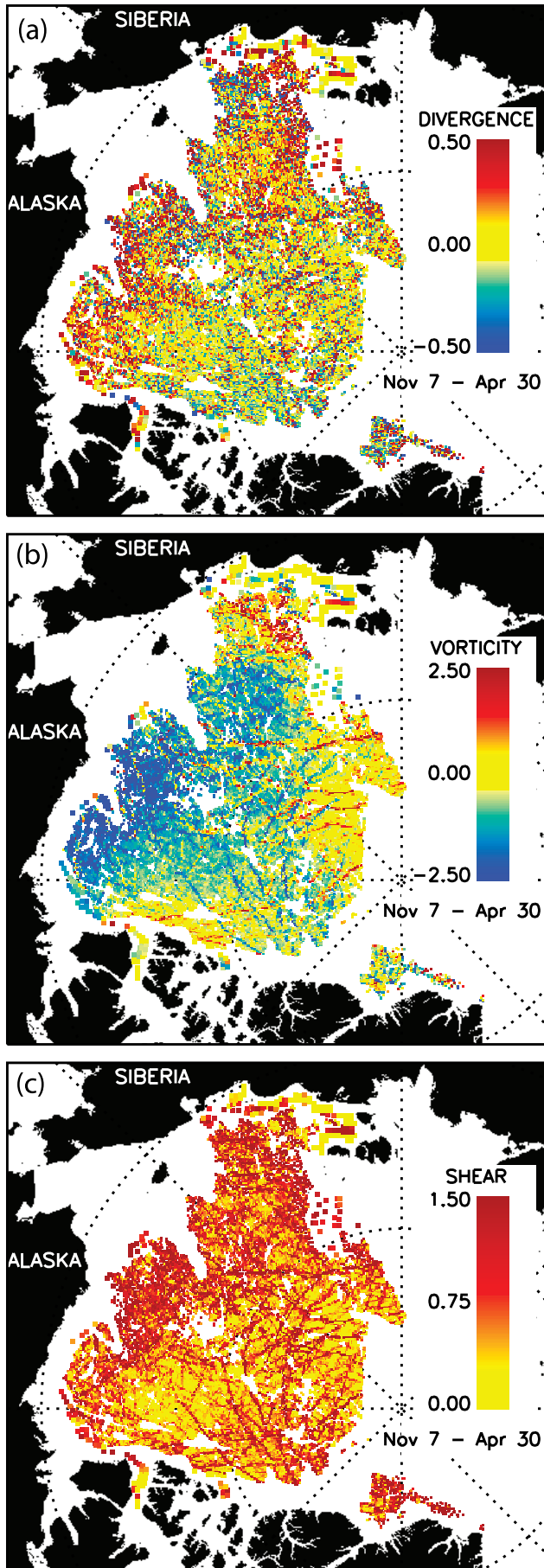


**Figure 2.** The number of observations and average sampling period for cells with observations over the period November 1996 through April 1997. Only cells with observations throughout the 6-month period are included in our analysis. The holes are observations with incomplete records due to data gaps or tracking difficulties. (a) The number of observations of each cell between November 1996 and April 1997; the map shows the spatial coverage of the cells on 7 November 1996. (b) The average sampling period of each cell and the spatial coverage of the cells on 30 April 1997.

over the period and then calculating the divergence, vorticity, and shear of the cell. The divergence, vorticity, and shear are measures of the cell area change, rotation, and deformation. This provides a broad spatial perspective of the deformation of the ice cover over 6 months. Most of the divergent cells are located south of  $80^\circ\text{N}$  in the Beaufort and



Chukchi Seas. The cumulative divergence of the cells in the central Arctic, north of  $80^{\circ}\text{N}$ , is smaller except for the activity of the cells west of the Canadian archipelago and north of the Greenland coast. The vorticity map shows a coherent rotation (anticyclonic) of the sea ice cover north of the Alaska coast that is an expression of the Beaufort Gyre. The net rotation of this region is over  $100^{\circ}$ . The remainder of the map shows translational motion. The shear field shows that the strongest shears are localized along linear features which are indicative of lead openings, ridging events or slip lines on the ice cover. Higher concentrations of these features are found in the lower latitudes close to the Alaska and Siberian coasts. The vorticity at each cell also provides a sense of the motion of the cell boundaries in shear. The length of some of these linear features is remarkable, as several can be seen to span a large fraction of the Arctic Ocean. These linear features also separate distinct areas with very little deformation.

### 2.3. Discussion of Ice Motion Errors

[13] A discussion of the ice motion/tracking errors are important since the accuracy of RGPS area and volume estimates are dependent on the reliable tracking of common ice features in SAR imagery. The uncertainties in ice displacement,  $u$ , and spatial differences derived from SAR imagery are discussed by *Holt et al.* [1992]. The standard error in  $u$  can be written as,

$$\sigma_u^2 = 2\sigma_g^2 + \sigma_f^2$$

where  $\sigma_g$  and  $\sigma_f$  are uncertainties in the geolocation of the image data and the tracking of sea ice features from one image to the next. This assumes that the additive errors are zero mean, normally distributed, uncorrelated random processes. Locally, where the geolocation errors between two images are correlated when the points are close together, the calculation of spatial differences to determine deformation is no longer dependent on the geolocation error of the data and the error tends to  $2\sigma_f^2$ . Comparison of RGPS and buoy displacements gives an RMS difference of  $\sim 300$  m. This is a measure of  $\sigma_u$  only if the buoy positions are absolutely correct. Of course, this is biased by buoy location errors as well. A detailed description of this comparison is given by *Lindsay et al.* [2000] (also available at <http://psc.washington.edu/>). This value of  $\sigma_u$  places an upper bound on  $\sigma_f$  which is important in understanding the error in area calculations discussed in the next section.

### 3. Area of the Ice Cover

[14] In the following analyses, we divide the initial region into five subregions (Figure 4) to examine the large-scale variability and relative contribution of each subregion to the area change, seasonal ice volume production, and multiyear ice. Henceforth, we designate subregion  $i$  as  $S_i$ . The sea ice cover of the Beaufort, Chukchi, and East Siberian Seas in

**Figure 3.** (opposite) The cumulative divergence, vorticity, and shear of the cells over the period 7 November 1996 through 30 April 1997. (a) divergence, (b) vorticity, (c) shear. (Units: /6 months) The cells are shown at their locations on 30 April.

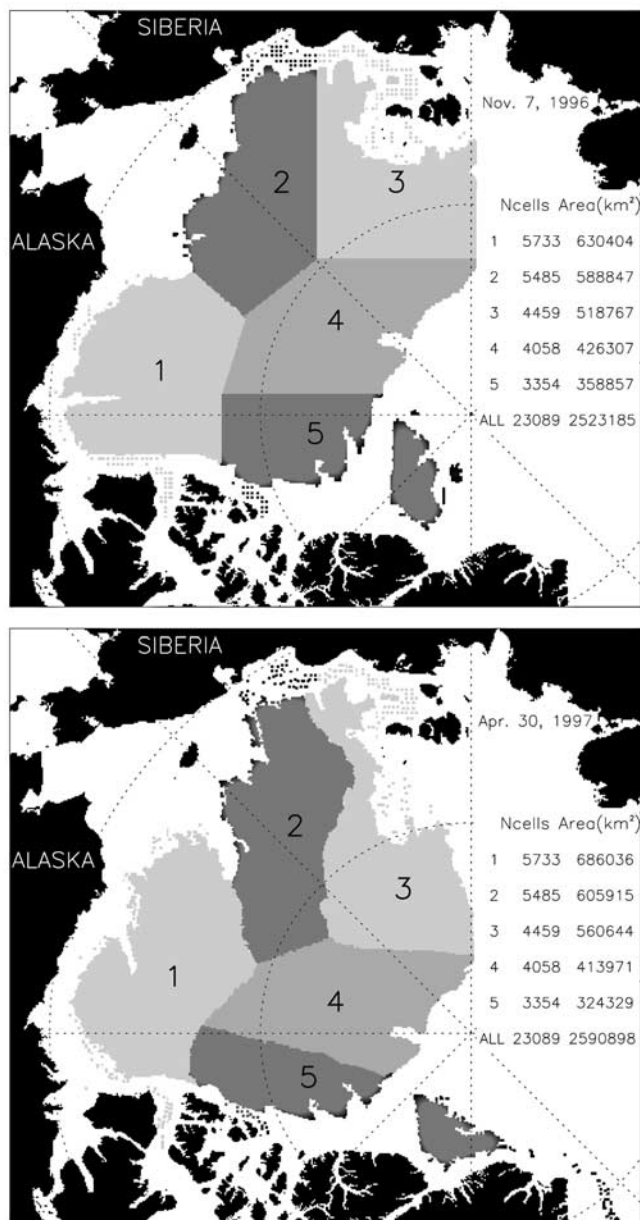


**Figure 4.** The spatial coverage of the five subregions ( $S_1$ – $S_5$ ). (a) 7 November 1996. (b) 30 April 1997. The areas of the subregions and the number of cells in each subregion are also shown.

$S_1$ ,  $S_2$  and  $S_3$  have larger fractions of multiyear ice in the north and higher concentrations of first-year ice in the south. The central Arctic and Canada Basin ice covers ( $S_4$  and  $S_5$ ) generally have higher fractions of multiyear ice. First, we discuss the total area of the ice cover in the region sampled by the RGPS cells. The total area of a region at each time step is the sum of the area of all cells within that region. Again, cells that are not observed throughout the period are not included in the calculations. Table 1 summarizes the changes in the area and volume characteristics of each subregion over the season. Figure 4 shows the area covered by the RGPS cells at the beginning and at the end of the period. On 7 November 1996 there are 23,089 cells covering

an area of  $2.52 \times 10^6$  km<sup>2</sup> or  $\sim 36\%$  of the Arctic Ocean. At the end of the period (30 April 1997), the same cells cover an area of  $2.59 \times 10^6$  km<sup>2</sup>, a net divergence of  $\sim 3\%$ . The sequence of area change (Figure 5) shows periods of net divergence and convergence over the 6-month period.

### 3.1. Time-Series of Area Change: Five Subregions

[15] Since the subregions are covered by RGPS cells, we are able to follow their motion and deformation over time. Over the 6-month period,  $S_1$  and  $S_2$  advected west towards Siberia as part of the Beaufort Gyre. The southern boundary of  $S_3$  next to the New Siberian Islands has pulled away from the Siberian coast and moved north toward the Pole.  $S_4$  remained relatively undeformed but rotated clockwise with the Beaufort Gyre. Its western boundary moved toward the Pole as part of the Transpolar Drift Stream.  $S_5$  shows a noticeable zonal compression as a result of the convergence of the ice cover on the Canadian archipelago. Part of  $S_5$  has been broken off and advected eastward. Some of these cells from  $S_5$  have actually exited the Arctic Ocean through the Fram Strait. Overall, there are net increases in area in  $S_1$  (9%),  $S_2$  (3%), and  $S_3$  (8%) and net decreases in area in  $S_4$  (–3%) and  $S_5$  (–10%) (see Table 1).

[16] The time series of area change of the five subregions are shown in Figure 5. A convergence event in late November affected all the subregions except  $S_3$ . The area record of  $S_1$  varies the most, with a range of  $\pm 10\%$ , and explains a large percentage of the area variability of the entire region. The area changes of the other subregions are less remarkable. The distributions of the area changes of cell population every 6 days are shown in Figure 6a. As expected, most of the deformations are localized along leads while large fractions of cells have very small divergence ( $|\alpha| < 0.5\%/day$ ) as the remainder of the ice cover remains rigid. The late-November convergence of the ice cover (mentioned earlier) can be seen as an increase in the number of cells with divergence  $< -2\%/day$ . This is especially evident in  $S_1$  and  $S_5$ . Over the 6-month period, the contrast in the number of cells with net increases in area and net decreases in area is indicative of the net area change of each subregion. In all the subregions, the fraction of cells having very small divergence ( $|\alpha| < 0.5\%/day$ ) increases with time. This suggests that as the ice cover gets thicker and stronger through the winter, as there is less deformation within the cell population.

### 3.2. Uncertainty in Area Calculations

[17] An approach to obtain an estimate of the expected errors in area calculations,  $\sigma_c$ , due to tracking anomalies can be done by examining the distribution of area changes of the cell population. The assumption here is that most cells remain rigid and deformation is localized along leads. Thus, the standard deviation of the fractional area change of all rigid cells provides a reasonable indication of the tracking noise. Figure 6b shows the standard deviation of the daily fractional area change of the entire cell population in the five subregions. With the understanding that this statistic is biased by actual cell deformations since it includes all cells and not just rigid cells, the standard deviation places an upper bound on the uncertainty of the area change calculations due to tracking errors. The standard deviation varies between 0.5%/day and 1.0%/day. A negative temporal trend in the standard deviation is again indicative of a thicker and

**Table 1.** Coverage of Sea Ice and Multiyear Ice, and Volume Stored in Seasonal Ice Within the Five Subregions Shown in Figure 4

	S <sub>1</sub>	S <sub>2</sub>	S <sub>3</sub>	S <sub>4</sub>	S <sub>5</sub>	Total
RPGS sampling						
Number of cells	5,733	5,485	4,459	4,058	3,354	23,089
Cells with increases in area (cumulative)	3,239	2,836	2,425	1,632	934	11,066
Cells with decreases in area (cumulative)	2,494	2,649	2,034	2,426	2,420	12,023
Area (10 <sup>3</sup> km <sup>2</sup> )						
Initial area (4 Nov. 1996)	630	589	519	426	359	2,523
Final area (30 April 1997)	686	606	561	414	324	2,591
Area change (Final–Initial)/Initial, %	8.8	2.9	8.1	–2.9	–9.6	2.7
Undeformed/Ridged ice coverage on 30 April, %						
(Ridging only)						
Undeformed ice	28	26	25	12	13	22
Ridged ice	5	4	3	2	3	4
Ridged first year (FY <sub>r</sub> )	7	8	6	5	7	6
Total ridged ice coverage	12	12	9	7	9	10
(Ridging/Rafting)						
Undeformed ice	21	21	17	10	13	18
Ridged ice	8	9	7	4	5	7
Ridged first year ice (FY <sub>r</sub> )	7	8	6	6	8	7
Total ridged ice coverage	15	17	13	10	13	14
Volume production (November through April)						
(Ridging only)						
Volume in undeformed ice, km <sup>3</sup>	184	135	110	42	34	505
Average thickness of undeformed ice, m	1.05	0.88	0.85	0.80	0.74	0.90
Volume in ridged ice, km <sup>3</sup>	59	47	34	19	21	180
Average thickness of ridged ice, m	1.92	1.83	1.87	1.98	2.12	1.91
Total volume (undeformed + ridged), km <sup>3</sup>	244	182	143	61	55	685
Volume in ridged first year (estimated) <sup>a</sup>	81	82	55	41	51	309
Total volume (undeformed + ridged + FY <sub>r</sub> ), km <sup>3</sup>	324	264	199	103	106	994
Average thickness (undeformed + ridged + FY <sub>r</sub> )	1.30	1.18	1.12	1.24	1.32	1.22
(Ridging/Rafting)						
Volume in undeformed ice	147	103	82	31	27	390
Average thickness of undeformed ice	1.09	0.81	0.85	0.72	0.63	0.85
Volume in ridged ice	88	75	52	28	27	270
Average thickness of ridged ice	1.68	1.45	1.53	1.49	1.48	1.53
Total volume (undeformed + ridged)	234	178	134	59	55	660
Volume in ridged first year (estimated) <sup>a</sup>	70	70	47	35	42	263
Total volume (undeformed + ridged + FY <sub>r</sub> ), km <sup>3</sup>	304	248	181	95	97	923
Average thickness (undeformed + ridged + FY <sub>r</sub> )	1.33	1.09	1.12	1.10	1.07	1.14
Multiyear (MY) ice						
Average MY ice area (10 <sup>3</sup> km <sup>2</sup> )	432	475	471	385	320	2,083
Fractional coverage relative to initial area, %	69	81	91	90	89	83
MY ice area - standard deviation (10 <sup>3</sup> km <sup>2</sup> )	12	10	6	7	7	35
Fractional change in area over 6 months, %	–5	–3	–2	–5	–7	–4

In the ridging/rafting case, ridge ice includes ridged and rafted ice.

<sup>a</sup>Volume in ridged first-year ice = Average thickness of ridged ice × Area of ridged first-year ice.

more rigid ice cover after several months of ice growth. We also note that the standard deviation approaches a value  $\sim 0.5\%$ /day in all the regions.

[18] Numerical simulation of tracking errors shows that normally distributed random displacements with standard deviations of 100 m, 200 m, and 300 m introduce errors ( $\sigma_c$ ) of 1.4%, 2.8%, and 4.0% in the area calculations. These errors in opening and closing do not depend on the time interval between observations. Since the typical average sampling period is three days, these are equivalent to divergence errors of 0.5%/day, 0.9%/day, and 1.3%/day. Thus, it seems that the tracking errors,  $\sigma_f$ , are much smaller than the  $\sigma_u$  obtained by comparison with buoy ( $\sim 300$  m) discussed earlier. This suggests that errors in tracking,  $\sigma_f$ , are on the order of 100 m or 1 pixel - the quantitation level of geographic location of grid points in the RGPS. With this level of error in cell area calculations, the expected error in the divergence estimate of a region with  $N$  cells would be

$0.005/\sqrt{N}$  (/day). For an area of 100 km by 100 km that is covered with 100 cells, this error would be 0.05%/day, giving us extremely high confidence in the divergence calculations.

#### 4. Ice Volume Production

[19] The cell ice thickness distributions,  $g_s(h)$ , are dependent on ice growth and the assumed mechanical redistribution of sea ice during convergence. The ice growth model used in the RGPS is described earlier. Recent studies [Hopkins *et al.*, 1999], emphasized the importance of both rafting and pressure ridging when two ice sheets are pushed together. Here, we compare the volume production and thickness distributions (see Figure 10) using two thickness redistributors with: (1) pressure ridging only (where  $k = 5$ ) and (2) combination of rafting (where  $k = 2$  for  $h \leq 40$  cm) and pressure ridging ( $k = 5$  for  $h > 40$  cm). In the first case, all ridged ice is five times its original thickness and

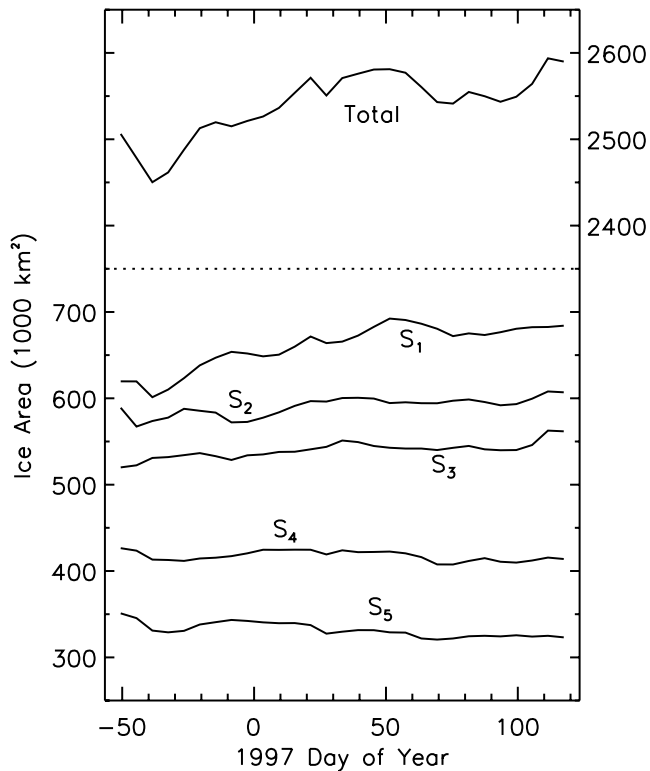


**Figure 5.** The time-series of area changes of the five subregions ( $S_1$ ,  $S_2$ ,  $S_3$ ,  $S_4$ , and  $S_5$ ).

occupies a quarter of the area. In the second case, ice less than 40 cm thick is rafted instead of ridged. The consequences of the two approaches used to account for decreases in cell area are discussed below. Currently, only the rafting/ridging results are available in the RGPS products.

[20] The entire thickness distribution in an RGPS cell is not known a priori. During closing events, when the known ice volume in the thickness distribution,  $g_s(h)$ , has been exhausted in the ridging/rafting process, the sea ice in the remainder of a cell is ridged. To account for the coverage of ridged areas of unknown thickness, a separate category called area of FY-ridges ( $FY_r$ ) is maintained in the RGPS record. This allows us to keep track of the coverage FY-ridges over a cell, even though the volume stored in these  $FY_r$  are not known.

#### 4.1. Seasonal Thickness Distribution and Volume Production

[21] Table 1 summarizes the mean ice thickness and volume production at the end of the period. Figure 7 shows  $g_s(h)$  of the five subregions at the end of April produced by the two redistributors. For the two cases, the evolution of the ice thickness distribution, the area coverage by undeformed and ridged ice, and volume production over the 6-month period are shown in Figures 8, 9, and 10. We first discuss the results for the case with only pressure ridging before we contrast the results between the two redistributors.

##### 4.1.1. Pressure Ridging Only

[22] Over the entire region, the coverage by thin ice between 0 and 20 cm is typically less than 2% (Figure 8). This is the most crucial thickness range that produces the most

ice growth, the most turbulent heat flux to the atmosphere and the most salt flux to the ocean. On the average,  $S_1$  and  $S_2$  have larger fractions of sea ice in the 0–20 cm range when compared to  $S_4$  and  $S_5$ . The undeformed ice in  $S_1$  covers ~28% of the area at the end of April (Table 1) while  $S_4$ , a region of net convergence over the 6-month period, has the smallest at 12%. Undeformed ice occupies ~22% of the total area. The average thickness of undeformed ice over the region is ~0.9 m, with the average thickness highest in  $S_1$  (1.05 m) and lowest in  $S_5$  (0.74 m). The undeformed ice in  $S_5$  is thinner probably because thinner ice categories created by recent openings lower the average. At the end of April, the total volume stored in undeformed ice is ~505 km<sup>3</sup>.

[23] Ridged ice covers ~10% of the area at the end of April. 60% of that area is covered by  $FY_r$  and is a direct result of ridging ice area of unknown volume and thickness. As mentioned earlier, this is a consequence of not knowing the initial thickness distribution of each cell.  $S_1$  has the largest fractional coverage of ridged ice while  $S_4$  has the smallest. The average thickness of ridged ice of the region is 1.9 m containing a volume of ~180 km<sup>3</sup>. Not surprisingly, the thickest ridged ice is found in  $S_5$ , off the Canadian archipelago. To obtain an estimate of the total ice volume stored in undeformed ice, ridged ice, and  $FY_r$ , we assume that the average thickness of the  $FY_r$  to be the same as that of ridged ice. With that assumption, approximately 994 km<sup>3</sup> (or 0.38 m) of ice is produced in the entire region over the 6 months. The highest volume production from the Beaufort region ( $S_1$ ) is three times that of the central Arctic Ocean ( $S_4$ ) (Figure 10). Ice volume production reflects the character of the ice dynamics in the region. Thermodynamic growth is highest in openings and undeformed ice areas. Ridging only serves to redistribute ice into thicker categories resulting in slower growth rates. Thus, the variability of divergence in  $S_1$  contributes to the abundance of undeformed ice and the resulting volume production.

##### 4.1.2. Ridging/Rafting

[24] Here, we contrast the results obtained using a redistributor with rafting with the ridging-only results above. Figures 9 and 10 show clearly the regional differences in the coverage and volume stored in undeformed and deformed ice obtained from the two schemes. At the end of April, undeformed ice covers 21% of the area, 7% less than the case with only pressure ridging. The total deformed (ridged/rafted) ice coverage is now more comparable to that of undeformed ice. The average thickness of undeformed ice from the two cases, however, is not significantly different as this is controlled almost entirely by thermodynamics. With rafting, there is remarkably less undeformed ice coverage because rafting consumes more undeformed ice area than ridging. The significant difference is in the average thickness of ridged ice at 1.68 m compared to the 1.92 m in the case with only pressure ridging. Rafted ice is much thinner and therefore biases the average towards the thin end of the distribution.

[25] The total ice volume produced in the five regions is ~7% less than before, 923 km<sup>3</sup> compared to 994 km<sup>3</sup>, even though the mechanical redistributors are different. Their average thicknesses are similar, at 1.14 m and 1.22 m. The decrease in ice production is expected. For a given unit of convergence of a uniform ice slab, more undeformed thin ice

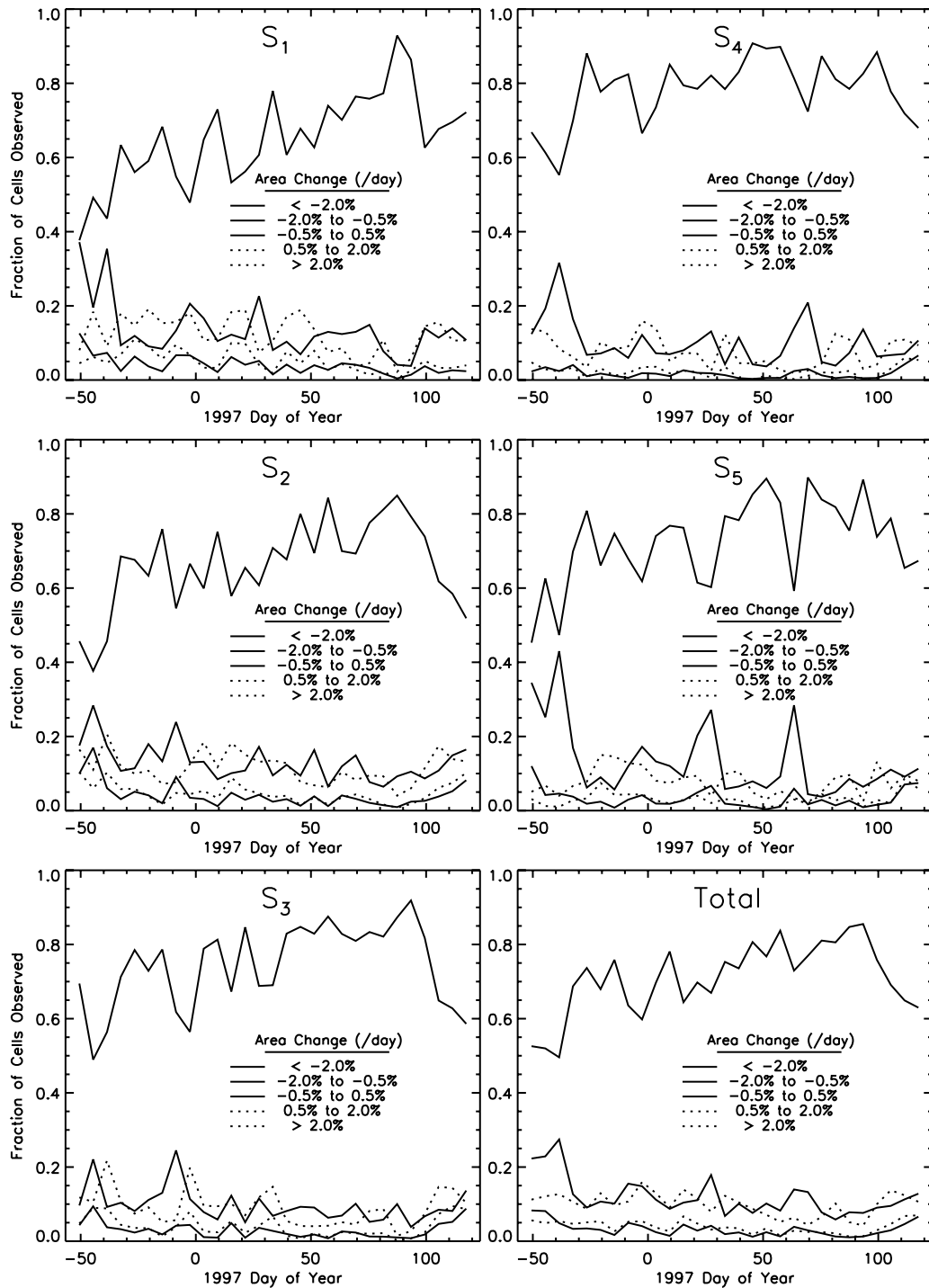


**Figure 6.** Distribution of cell area changes within the five subregions at each time step. (a) Fractional area change  $S_1$  through  $S_5$  (%/day). (b) The standard deviation of area changes of the cell population (%/day).

remains after ridging than rafting because the ridging process piles the ice up into smaller effective areas leaving larger areas of thin ice unaffected. Since the growth rate of thinner ice is higher, we expect more ice production due to thermodynamic growth in the case with only pressure ridging. On the other hand, rafting creates more thinner deformed ice, thus allowing more rapid ice growth under the thinner rafted ice. The balance of dynamics and thermodynamics reduces this difference in ice production. The most significant differ-

ence between the two cases is the coverage of deformed versus undeformed ice as seen in Figure 10.

#### 4.2. Uncertainty in Volume Calculations

[26] The potential error sources associated with volume and thickness estimates: temporal sampling; spatial sampling; noise in area changes; and ice growth/ridging model are discussed here. The noise in the area change record is a consequence of ice motion tracking errors. We note at the

### Ice Area Change

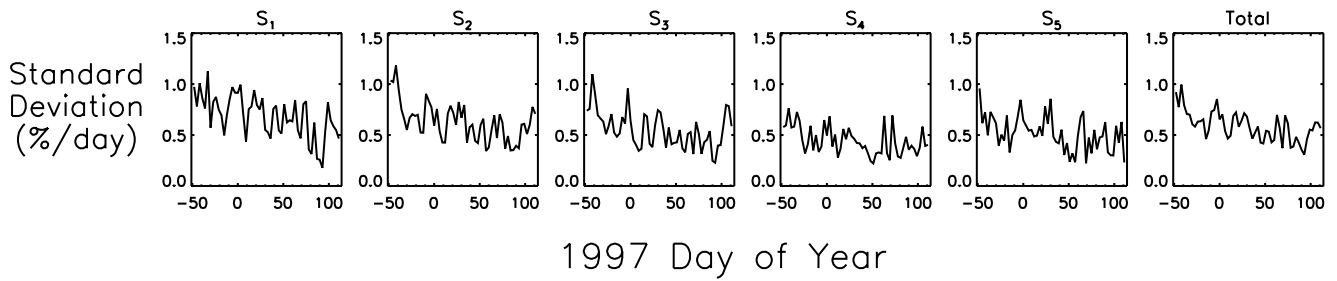


Figure 6. (continued)

outset that the choice of the frequency of temporal and spatial sampling of the RGPS cells is determined by data acquisition strategy and data processing throughput. The limitations of sampling processes have a number of implications on ice thickness and volume estimates. The growth/ridging models

are selected based on their simplicity in parameterization of these processes.

#### 4.2.1. Noise in Area Estimates

[27] The noise in cell area estimates (discussed above) introduces an uncertainty in the area coverage and thus the

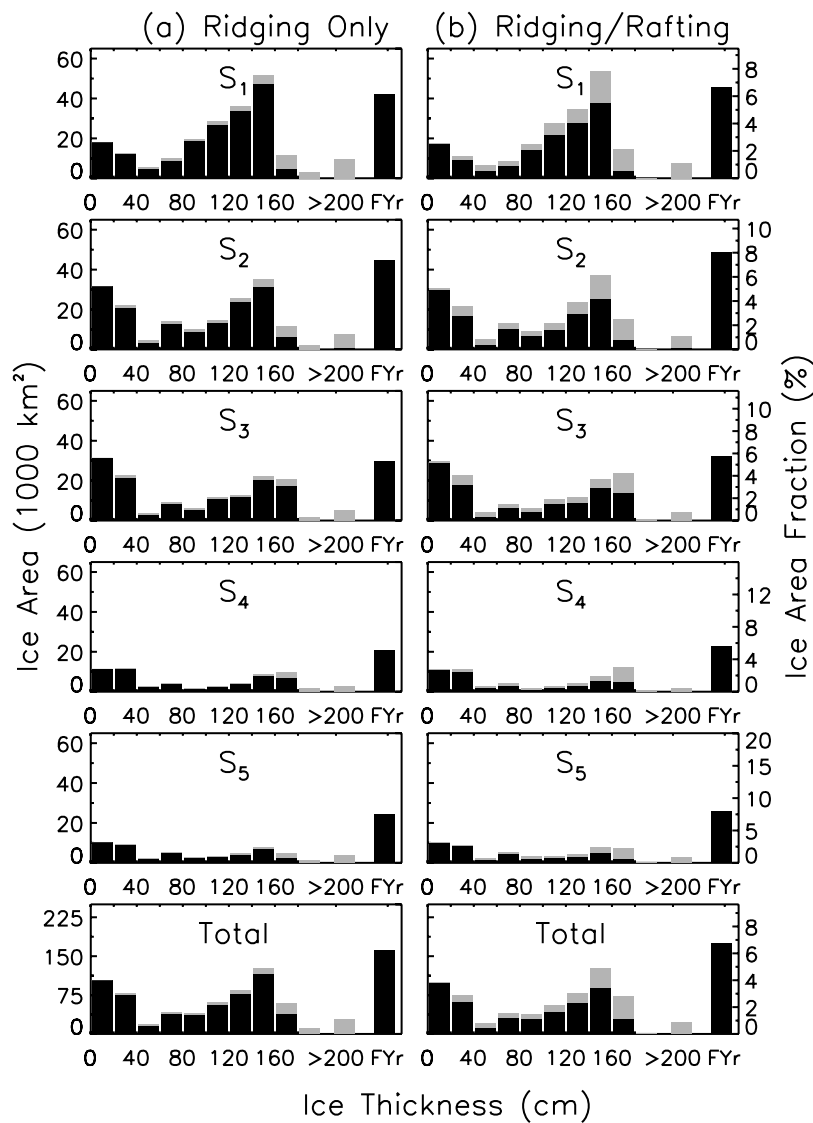
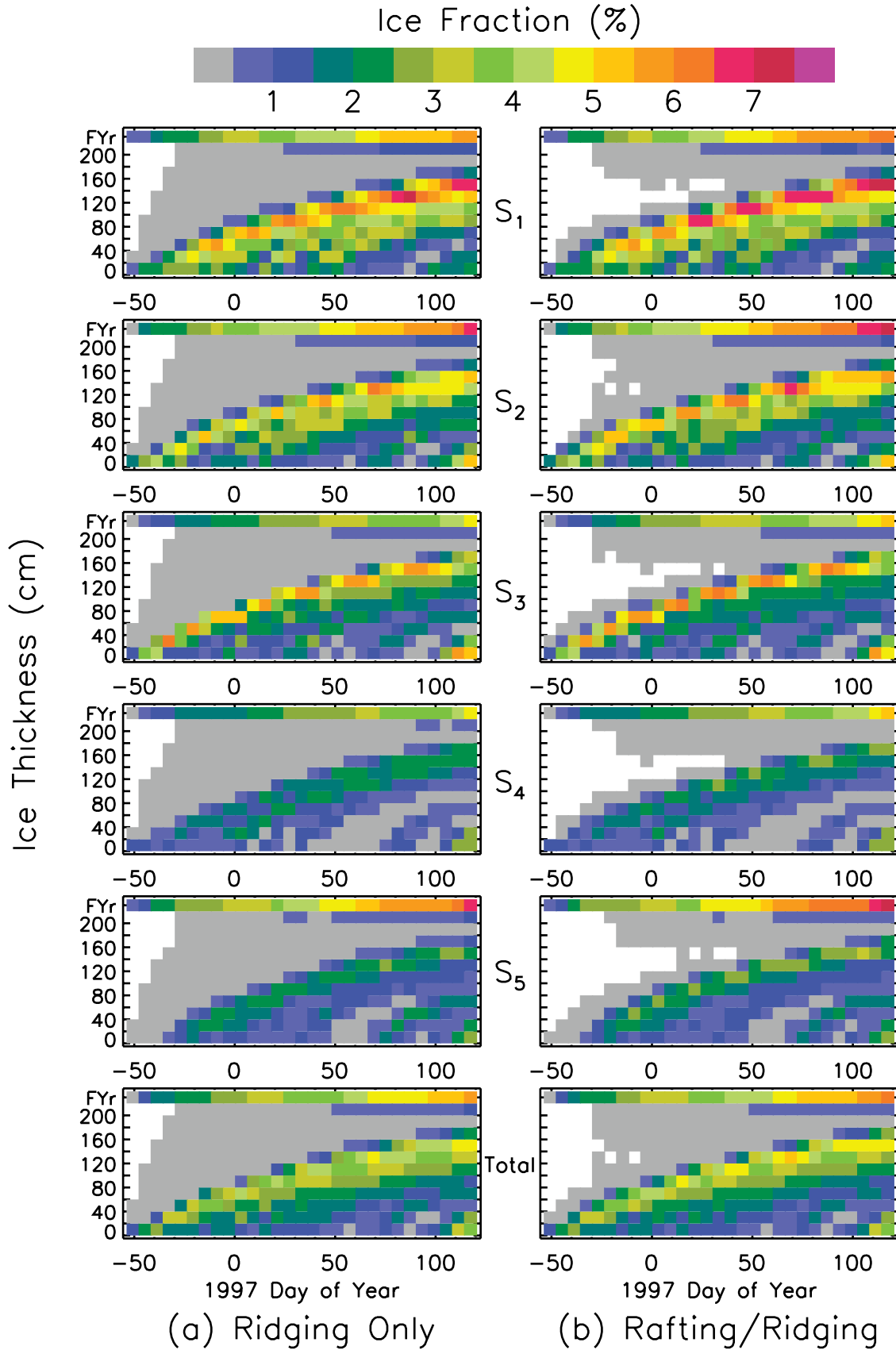
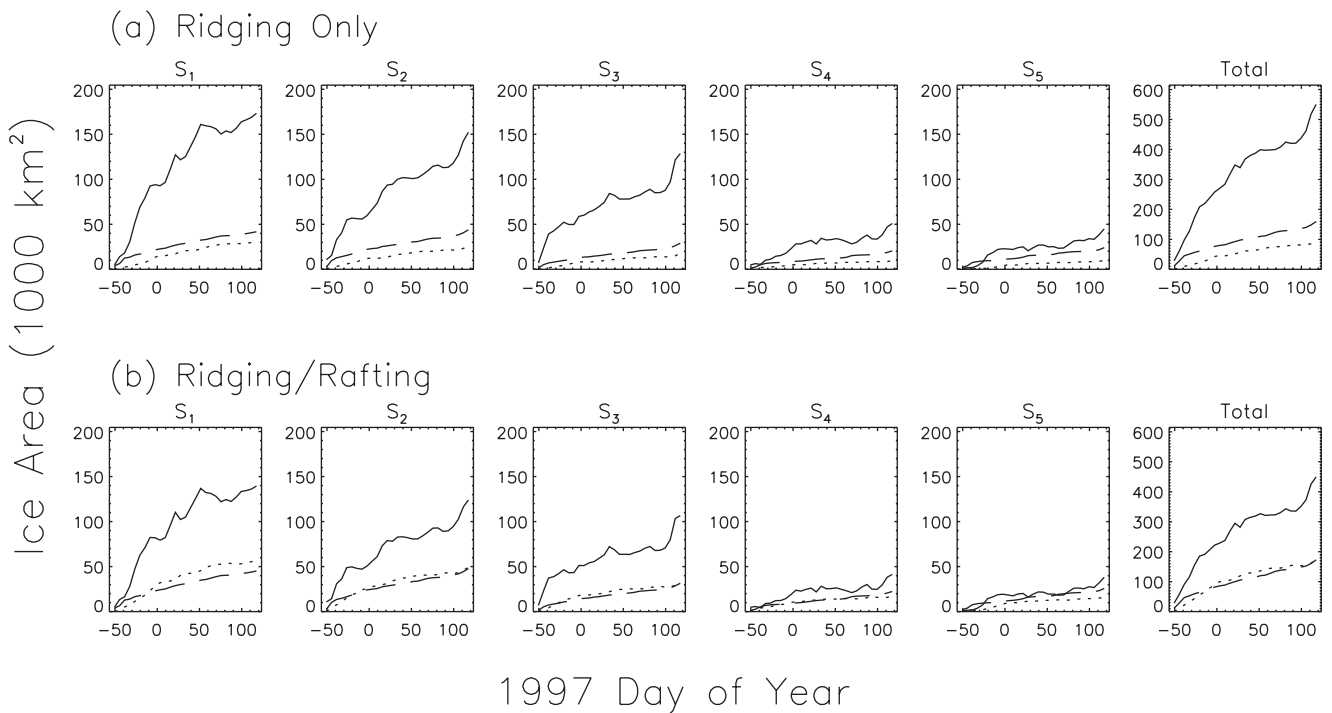


Figure 7. The seasonal ice thickness distribution,  $g_s(h)$ , in the five subregions at the end of April, 1997. (a) Ridging only. (b) Ridging/rafting. The coverage of ridged/rafted ice is shown in light gray. The area of FY-ridges (FY<sub>r</sub>) is shown as a separate category.



**Figure 8.** Evolution of the  $g_s(h)$  over the 6-month period in the five subregions. (a) Ridging only. (b) Ridging/rafting. The  $g_s(h)$  are plotted at 6-day time steps.



**Figure 9.** Coverage of seasonal ice (solid line), ridged ice (dotted line), and FY-ridges (FY<sub>r</sub>, dashed line) over the 6-month period in the five subregions. (a) Ridging only. (b) Ridging/rafting.

volume production in each cell. In the mean, this error adds an uncertainty of 1.5% of the area of the cell to the actual opening and closing of the cell over the 3-day sampling period. Random openings and closings contribute positively to the volume production and seasonal thickness

distribution. Numerical simulation, using a constant air temperature of  $-25^{\circ}\text{C}$  for ice growth and a pressure-ridging only redistributor, shows that normally distributed random errors in area calculations with standard deviations of 1.5% and 2.0% provide an estimate of the biases in ice

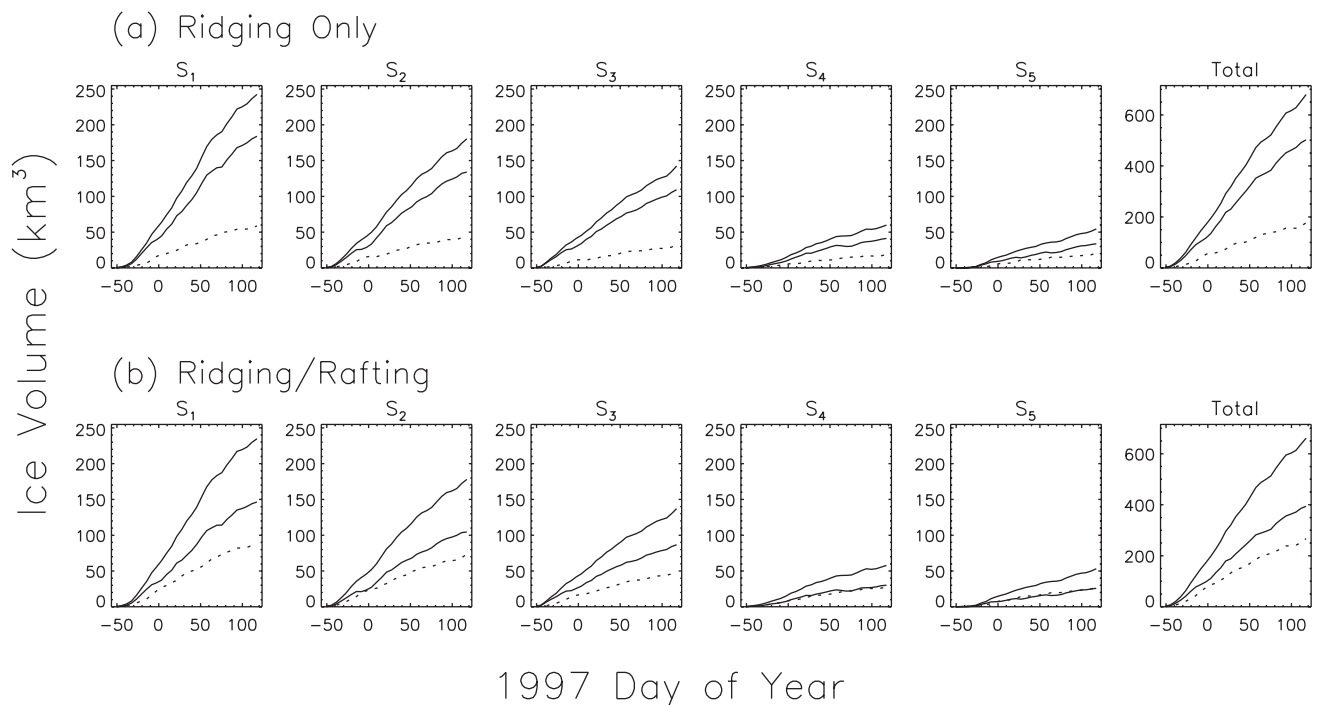


**Figure 10.** Seasonal sea ice volume stored in seasonal ice (thin solid line) and ridged ice (dotted line), and the total ice volume (thick solid line) over the 6-month period in the five subregions. (a) Ridging only. (b) Ridging/rafting.

volume production. Over 6 months and an area covered by 23,089 cells ( $\sim 2.52 \times 10^6 \text{ km}^2$  - approximately the area of the region here), the volume is overestimated by  $5 \text{ km}^3$  and  $7 \text{ km}^3$ , less than 1% of the  $\sim 1000 \text{ km}^3$  produced over the period. The area noise does not contribute significantly to the volume production or the thickness distribution. Most of the volume created by the noise in area calculations is stored in ridged ice because the zero-mean noise process tends to pile-up undeformed ice created during previous time steps.

#### 4.2.2. Temporal Sampling

[28] All the RGPS cells are surveyed nominally once every three days and the area changes observed are actually net changes over that interval. This temporal sampling strategy of the cell area record means that opening and closing events over the interval resulting in zero net area change would be missed. An opening followed by closing within a three-day interval would introduce an ice volume stored in ridged/rafted ice that is unaccounted for in the RGPS record. Similarly, a closing followed by an opening result in unaccounted for volume in ridged/rafted ice and the introduction of an undeformed ice area. The consequence is then an underestimation of the sea ice volume produced over a 3-day period. The 3-day sampling represents the length scale of synoptic storms in the Arctic Ocean. However, there does not exist an adequate data set to allow us to quantify the magnitude of this uncertainty. The magnitude of the error would be dependent on the size of the open leads that are missed.

[29] Also associated with the 3-day sampling is the uncertainty in the exact time of occurrence of an opening or closing event. Using the ice growth model here, a sampling interval of three days would cause an average uncertainty in ice age of  $\sim 1.5$  days or an uncertainty in the thickness of the thinnest ice of about 12 cm assuming an air temperature of  $-30^\circ\text{C}$ . As the ice gets thicker, the growth rate slows and the uncertainty in thickness decreases.

#### 4.2.3. Spatial Sampling

[30] We assume that the cell boundaries are defined by straight-line segments connecting the cell vertices. The sides of these cells are not the actual boundaries of the material element. Floes smaller than the cell dimensions could advect in and out of these boundaries. Inspection of SAR imagery shows that this does not happen often since most deformations are along leads between rigid plates during the winter and independent motion of small floes are not observed. An associated spatial sampling issue is that the area change of a cell is interpreted as caused by a single type of event - opening or closing. If there is a mix of opening and closing events within the 10 km by 10 km cell producing the same net area change, these events would not be sampled correctly.

[31] The ice motion field is not a continuous, differentiable field since the deformation is localized along linear features. At discontinuities, (e.g., slip lines, leads) sometimes unfavorable geometric location of the grid points relative to these linear features would lead to inadequate spatial sampling of the deformation and cause spurious openings and closings of the ice cover. The errors introduced in this case would be dependent on the direction of the discontinuity relative to the orientation of the sampling grid. The effect would cause an overestimation in the volume production.

#### 4.2.4. Ice Growth/Ridging

[32] Ideally, a full surface energy balance model could be used to estimate ice growth. The models used in this study were selected for their simplicity such that results could be easily interpreted. Lebedev's parameterization using freezing-degree days describes ice growth under "average" snow conditions. Snow thickness affects growth rate, but there are no routine measurements available for use in the RGPS. Wind speed is also an important factor. It is clear that there would be a bias in the volume production based on the actual snow cover, meteorological conditions, and different growth parameterizations. The mechanical redistribution of ice is based on anecdotal evidence, and there are a number of models that could be used. Two schemes are examined here to assess the sensitivity of the results to simple parameterizations.

#### 4.3. Remarks on Validation of the RGPS Ice Thickness

[33] A record of the available estimates of annual sea ice growth and melt in the central Arctic Ocean are summarized in Table 1 in *Steele and Flato* [2000]. The only mass balance observations that are taken along a transect of varying ice thickness [*Koerner*, 1973] give an annual growth of  $\sim 1.1$  m. This annual mean approximately doubles that of the growth estimates over that for 3 m ice of  $\sim 0.5$  m [*Untersteiner*, 1961]. Since we estimate only the growth of seasonal ice, our estimate should be comparable to that of the difference between the two estimates above (i.e.,  $1.1 \text{ m} - 0.5 \text{ m} = 0.6 \text{ m}$ ). Indeed, scaling our growth estimate of  $\sim 0.38$  m from 6 to 8 months gives an annual growth estimate of  $\sim 0.5$  m. Thus, given the uncertainties in the above observations, our estimate is comparable to the above difference. Admittedly, this is a rather crude comparison but it does serve as a check on the reasonableness of our ice growth estimate.

[34] The present estimates of RGPS ice thickness and volume production require validation using current data sets from in situ and remote sensing measurements. Large-scale validation of Arctic Ocean processes has always been a challenge. Additional complications arise from the fact that the RGPS results only provide estimates of the seasonal ice thickness distribution rather than the entire distribution. Available data sets for thickness comparisons include ice draft data from submarine sonar measurements and ice thickness estimates from AVHRR data. Preliminary comparisons of AVHRR-derived ice thicknesses with RGPS-derived ice thickness estimates indicate reasonable agreement (Y. Yu, Thin ice in winter 1996/97 — Comparison between RGPS and AVHRR, 2000, in preparation). Also, Rothrock [personal communication, 2000] plans to compare submarine ice draft data with RGPS estimates. These validation efforts are crucial to the understanding of the RGPS results and the use of the RGPS data sets for future monitoring of the Arctic Ocean.

### 5. Multiyear Ice Coverage

[35] The RGPS uses a simple backscatter-based procedure [*Kwok et al.*, 1992] to classify a SAR image pixel as covered by one of two types of sea ice: multiyear or first-year. If ice that survives the summer is correctly classified as multiyear ice, then the multiyear ice coverage during the winter should

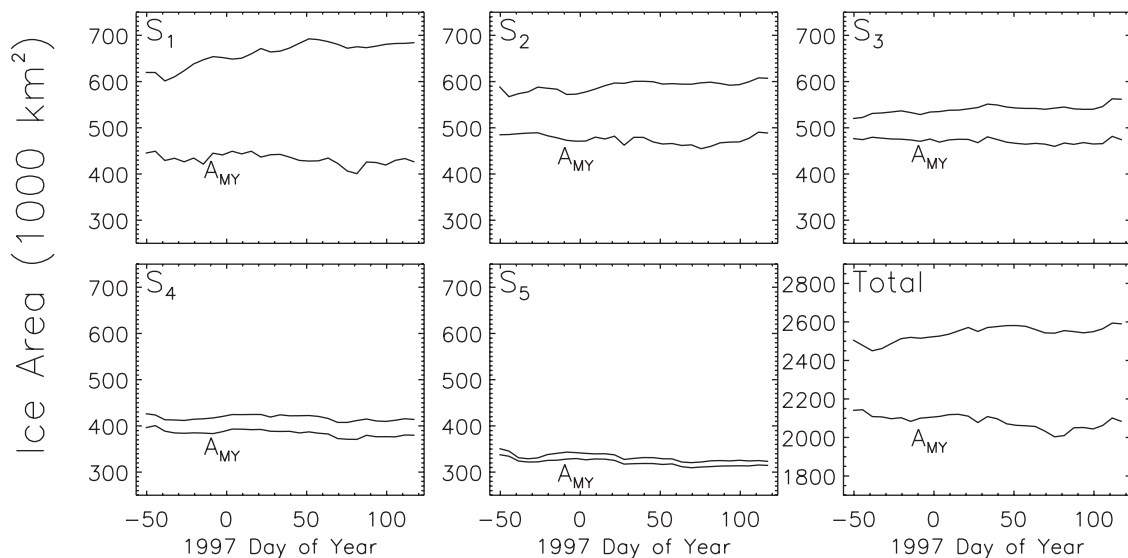


**Figure 11.** The area record of the five subregions (heavy dark line) and the RGPS-derived multiyear ( $A_{MY}$ ) coverage (lighter line).

be nearly equivalent to the ice concentration of the previous summer's minima, differing by an amount due to melt, ridging, and export of ice from the Arctic. As we consider the MY ice in Lagrangian elements in the winter, ice export and melt are not issues in the winter MY area balance in RGPS cells. Since no multiyear ice is created during the winter, we expect that the MY ice coverage within a Lagrangian region to remain constant and could only decrease due to ridging. This condition is a good test of whether the RGPS interpretation of the radiometry is sound. Certainly, the presence of wind-blown open water and frost flowers on thin ice have been shown to cause the ice classifier to overestimate the area of multiyear ice even though the winter signature of multiyear ice has been shown to be stable [Kwok and Cunningham, 1994]. These misclassification events can be identified as positive spikes or humps - noise in the retrieval process. A 6-month record of MY ice retrieval would allow us to filter out the noise to obtain the "background" or true multiyear ice area.

### 5.1. RGPS MY Retrievals

[36] Figure 11 shows the area change of the RGPS-derived multiyear ice coverage estimates for the entire region and for each of the five subregions. Table 1 shows the mean MY ice coverage, its variability, and the observed trend over the 6 months. Although a small negative trend is apparent, the  $A_{MY}$  in the five subregions stays fairly constant throughout the 6 months. Over the period, MY sea ice covers  $\sim 2.08 \times 10^6$  km<sup>2</sup> or 83% of the initial area of the entire region.  $S_1$  has the largest variability in MY ice area ( $\sim 12 \times 10^3$  km<sup>2</sup>) and the lowest concentration (69% relative to initial area) of MY ice. It is important to note that  $A_{MY}$  is reported here in actual area rather than fractional coverage since from a Lagrangian viewpoint any divergence or convergence would decrease or increase the fractional coverage.

[37] The total decrease in MY coverage over the 6 months is  $\sim 83 \times 10^3$  km<sup>2</sup> or  $\sim 4\%$  of the total  $A_{MY}$ . All subregions exhibit negative trends. The largest decrease can be seen in  $S_5$  (7%), the region of largest net convergence. We attribute

this decrease in  $A_{MY}$  to three factors: (1) the ridging of MY ice; (2) the piling of first-year ice onto MY ice during the ridging process; and (3) an actual trend in the MY ice signature due to changes in surface conditions (e.g., formation of hoar frost, thickness of snow cover, etc.). The ridging of MY ice is not unlikely at the end of the fall especially when the first-year ice that survived the summer, classified now as MY ice, may not be that thick. So, the conventional wisdom that MY area does not change throughout the winter may not be valid. But the expectation that only a small fraction of this ice participates in ridging should be valid. First-year ice definitely piles up onto MY ice during the ridging process, so this is not unexpected. However, there are no observational data that would allow us to quantify this effect.

[38] We discuss the third factor in more detail. Figure 12 shows the temporal dependence in the mean backscatter of all RGPS cells with more than 90% MY ice coverage. We sample this dependence at three different incidence angles. There is a negative trend ( $\sim 0.5$  dB over 6 months) in the data set. Over the same period, Kwok *et al.* [1999] report a slightly higher negative trend ( $\sim 1.5$  dB over 6 months) in Ku-band scatterometer data of the Arctic perennial ice. This trend was attributed to the development of hoar frost in the snow cover. If this is the cause of the trend, then an attenuated effect at C-band is expected since the lower frequency is less sensitive to snow cover properties. Regardless of the cause, would this effect lead to a negative trend in the MY ice retrieval? The classifier allows changes in the mean signature due to calibration uncertainties of  $\pm 1$  dB. The classifier compensates for a small trend of this magnitude. We do believe that the trend is real, and that it is caused by a combination of the above factors although they may not be separable based on our current understanding of the data set.

### 5.2. Comparison With Seasonal Ice Coverage Derived From Kinematics

[39] Here, we compare the first-year ice coverage,  $A_{FY}$ , derived from radiometry with the seasonal ice coverage

derived from kinematics (results from section 3). If the  $A_{FY}$  ( $=A_{tot} - A_{MY}$ ) derived from radiometry is a reasonable estimate of seasonal ice coverage, then the seasonal undeformed ice coverage ( $A_s$ ) derived from the RGPS ice thickness product should never be greater than  $A_{FY}$ , or,  $A_{FY} \geq A_s$ . This is because  $A_{FY}$  should include all the undeformed seasonal ice that exists at the initial RGPS observation of the ice cover on 7 November 1996. Undeformed seasonal ice is first-year ice and is assumed to have the same radiometric signature as all first-year ice. The uncertainty lies in whether ridged ice has the radiometric signature of first-year ice or MY ice. This is dependent on spatial resolution of the sensor as well as the electromagnetic properties of ridged ice.

[40] Figures 13a and 13b compare the  $A_{FY}$  coverage with the coverage of seasonal ice, ridged ice and first-year ridges. The curves show how the deformed and undeformed ice develops throughout the season. In all subregions, the undeformed seasonal ice approaches that of  $A_{FY}$ . In the pressure ridging case, the undeformed seasonal ice area sometimes exceeds the coverage of  $A_{FY}$  but in the case with rafting the undeformed seasonal ice is always within the bounds of  $A_{FY}$ . Broadly speaking, this comparison shows that the  $A_{FY}$ , derived radiometrically, is at least consistent with our hypothesis i.e.,  $A_{FY} \geq A_s$ . It seems that the  $A_{FY}$ , and therefore  $A_{MY}$ , are not unreasonable estimates of the first-year and multiyear ice coverage of the ice cover.

[41] Our results are seasonally self-consistent, meaning they satisfy some basic assumptions about the ice cover. For instance, except for the small decrease in MY coverage, the area remains relative constant. No MY ice is created during the winter. Whether the MY ice retrieval is biased is still in question.

## 6. Conclusion

[42] In this paper we have summarized one aspect of the RGPS data set from one winter season between November of 1996 and April of 1997. The changes in area of the ice cover, the seasonal ice thickness distribution, and the MY ice coverage over the 6-month period are examined. In the RGPS, the area change of the ice cover and the MY ice coverage are obtained directly from ice motion and the backscatter fields. The seasonal ice thickness distribution is derived from the record of cell divergence using a presumed model of ice growth and a model for mechanical redistribution of sea ice. At the present time, we have different levels of understanding of the quality of these measurements.

[43] The area changes of the ice cover represent the best available estimates of ice cover divergence. For large regions (100 km by 100 km), the estimated error is only small fractions of a percent. On the small scale, the RGPS cells provide a dense spatial sampling of ice-cover deformation, giving the locations of all resolvable openings and closings at each time step. The areal coverage of thin ice in the openings is crucial to the calculation of ice growth, brine flux, and heat flux. For the first time, we have large scale measurements of the spatial distributions of closings over the ice cover. Lower resolution sensors (e.g SSM/I, AVHRR) typically extract thin ice concentrations, using radiometric information, and are not sensitive to closing events.

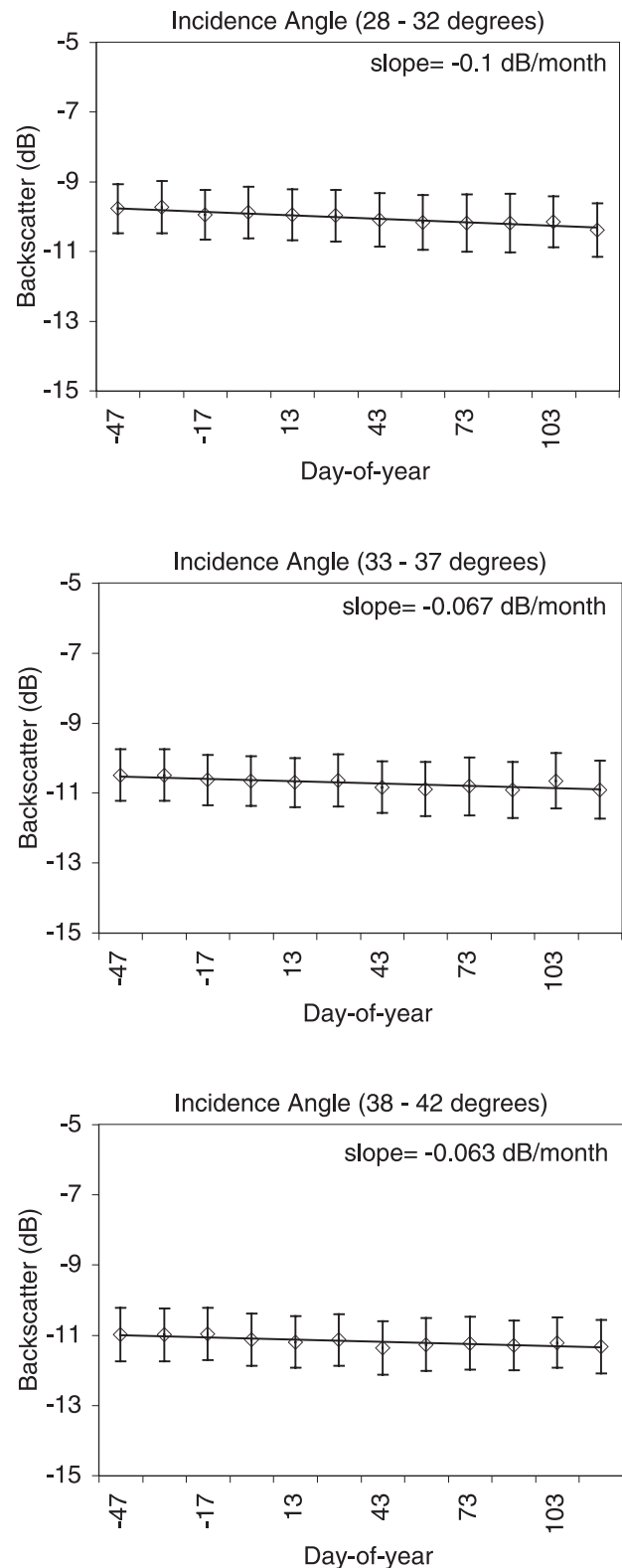


**Figure 12.** The changes in multiyear ice backscatter over the 6 months at three incidence angles.

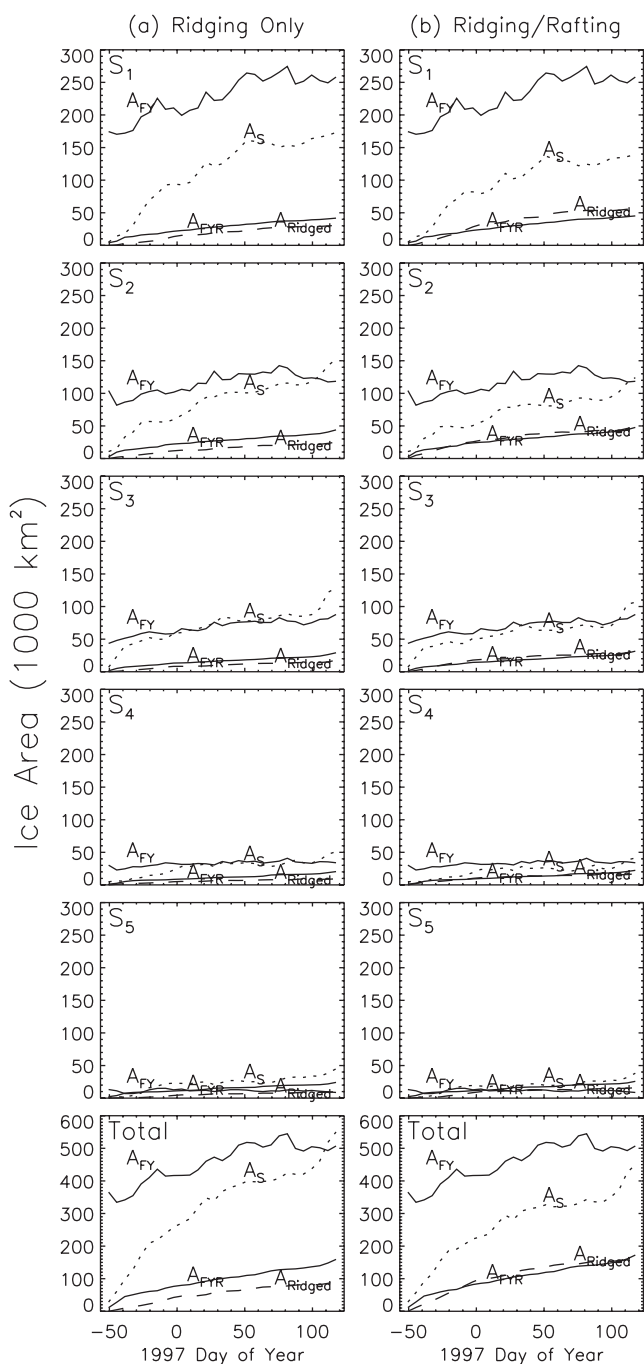


**Figure 13.** (a) The first-year sea ice ( $A_{FY}$ ) coverage derived from radiometry and the seasonal ice coverage ( $A_S$ ), the ridged ice coverage ( $A_{Ridged}$ ), and the FY-ridges ( $A_{FYR}$ ) coverage with only pressure ridging. (b) Same as (a) except with ridging and rafting.

[44] We have examined the seasonal ice thickness distribution and volume production using two different redistribution functions. In the RGPS data products, the contribution of the undeformed and ridged ice volumes to the total ice production can be separated. This provides insight into the dependence of the thickness distribution on regional ice dynamics. The ice production results obtained using two redistributors over the 6 months show an expected decrease when rafting is included in the thickness

redistribution. Our winter ice growth of  $1000 \text{ km}^3$  ( $\sim 0.4 \text{ m}$ ) is comparable to available observations. There are sources of uncertainty in the ice volume and ice thickness calculations that remain unquantified, but at this time there are no adequate in situ or remote-sensing data for a comprehensive evaluation of the above estimates. Several investigators are moving towards a comparison of the estimated ice thickness with AVHRR retrievals and submarine ice draft measurements.

[45] The retrieval of multiyear ice coverage, based entirely on backscatter, are consistent in that they remain near constant throughout the season, except for a small negative trend. The possible causes of these trends are examined. Also, comparison of the first-year ice coverage ( $A_{\text{tot}} - A_{\text{MY}}$ ) with the seasonal undeformed ice coverage indicates that they are at least consistent. That is, the coverage of the undeformed seasonal ice is lower than that of backscatter-derived first-year ice coverage. This provides confidence that the RGPS interpretation of the MY-backscatter is sound.

[46] At the RGPS spatial sampling of  $\sim 10 \text{ km}$ , we have a fine-scale description of the motion and deformation of the ice cover which can be put to a variety of applications. Here, we have restricted ourselves to the large-scale summary of area changes of the ice cover, seasonal ice thickness distribution, volume production, and MY ice coverage. The RGPS data set is also suited to the investigation of other small-scale processes. These geophysical products can be put to a variety of uses: analyzing new ice climatologies, testing ice models or new ideas about sea ice rheology, and for assimilating into sea ice models. This first season of RGPS products will also serve as a baseline for comparisons with data products to be produced in the coming years.

[47] **Acknowledgments.** The RADARSAT imagery are processed and calibrated at the Alaska SAR Facility, Fairbanks, AK. The RGPS is a joint project of the Alaska SAR Facility and the Jet Propulsion Laboratory. R. Kwok and G.F. Cunningham performed this work at the Jet Propulsion Laboratory, California Institute of Technology under contract with the National Aeronautics and Space Administration.

## References

- Fetterer, F., D. Gineris, and R. Kwok, Sea ice type maps from Alaska synthetic aperture radar facility imagery: An assessment, *J. Geophys. Res.*, *99*(C11), 22,443–22,458, 1994.
- Holt, B., D. A. Rothrock, and R. Kwok, Observations of sea ice motion from satellite imagery, in *Microwave Remote Sensing of Sea Ice*, *Geophys. Monogr. Ser.*, vol. 68, edited by F. D. Carsey, AGU, Washington, D. C., 1992.
- Hopkins, M. A., J. Tuhkuri, and M. Lensu, Rafting and ridging of ice sheets, *J. Geophys. Res.*, *104*(C6), 13,605–13,613, 1999.
- Koerner, R. M., The mass balance of the sea ice of the Arctic Ocean, *J. Glaciol.*, *12*, 173–185, 1973.
- Kwok, R., and G. F. Cunningham, Backscatter characteristics of the winter sea ice cover in the Beaufort Sea, *J. Geophys. Res.*, *99*(C4), 7787–7803, 1994.
- Kwok, R., E. Rignot, B. Holt, and R. G. Onstott, Identification of sea ice type in spaceborne SAR data, *J. Geophys. Res.*, *97*(C2), 2391–2402, 1992.
- Kwok, R., D. A. Rothrock, H. L. Stern, and G. F. Cunningham, Determination of ice age using Lagrangian observations of ice motion, *IEEE Trans. Geosci. Remote Sens.*, *33*(2), 392–400, 1995.
- Kwok, R., G. F. Cunningham, and S. Yueh, Area balance of the Arctic Ocean Perennial Ice Zone: Oct 1996–April 1997, *J. Geophys. Res.*, *104*(C11), 25,747–25,749, 1999.
- Li, S., Z. Cheng, and W. F. Weeks, A grid based algorithm for the extraction of intermediate-scale sea ice deformation descriptors from SAR ice motion products, *Int. J. Remote Sens.*, *16*(17), 3267–3286, 1995.

- Lindsay, R., H. Stern, D. A. Rothrock, Y. Yu, and R. Kwok, *Validation of RADARSAT Geophysical Processor System Products*, 2000.
- Maykut, G. A., The surface heat and mass balance, in *Geophysics of Sea Ice, Ser. B: Physics*, vol. 146, edited by N. Untersteiner, pp. 395–463, Plenum, New York, 1986.
- Overland, J. E., S. L. McNutt, and S. Salo, Arctic sea ice as a granular plastic, *J. Geophys. Res.*, 103(C10), 21,845–21,867, 1998.
- Parmeter, R. R., and M. Coon, Model of pressure ridge formation in sea ice, *J. Geophys. Res.*, 77, 6565–6575, 1972.
- Steffen, K., and J. Heirichs, Feasibility of sea-ice typing with synthetic aperture radar (SAR) — Merging of Landsat and ERS-1 imagery, *J. Geophys. Res.*, 99(C11), 22,413–22,424, 1994.
- Stern, H. L., D. A. Rothrock, and R. Kwok, Open water production in Arctic Sea ice: Satellite measurements and model parameterizations, *J. Geophys. Res.*, 100(C10), 20,601–20,612, 1995.
- Untersteiner, N., On the mass and heat budget of Arctic sea ice, *Arch. Meteorol. Geophys. Bioklimatol., Ser. A.*, 12, 151–182, 1961.
- 
- R. Kwok and G. F. Cunningham, Jet Propulsion Laboratory, California Institute of Technology, 4800 Oak Grove Drive, Pasadena, CA 91109, USA.